AGU PUBLICATIONS

JGR

Journal of Geophysical Research: Solid Earth

RESEARCH ARTICLE

10.1002/2014JB011092

Key Points:
- Repeating seismic experiments for monitoring velocity changes across Utah
- There is an observed and clear velocity change over a time period of 4 months
- Velocity changes might be due to the crustal deformation in the Basin and Range

Correspondence to:
C. Kanu,
ckanu@mines.edu

Citation:
Kanu, C., R. Snieder, and K. Pankow (2014), Time-lapse monitoring of velocity changes in Utah, *J. Geophys. Res. Solid Earth*, *119*, 7209–7225, doi:10.1002/2014JB011092.

Received 5 MAR 2014
Accepted 22 AUG 2014
Accepted article online 27 AUG 2014
Published online 29 SEP 2014

Time-lapse monitoring of velocity changes in Utah

Chinaemerem Kanu[1], Roel Snieder[1], and Kristine Pankow[2]

[1]Center for Wave Phenomena, Department of Geophysics, Colorado School of Mines, Golden, Colorado, USA, [2]University of Utah Seismograph Stations, Salt Lake City, Utah, USA

Abstract The Eastern part of the Basin and Range, extending to the Wasatch fault region, is an actively deforming region characterized by varieties of extensive features and prominent seismicity along the intermountain seismic belt. The present-day deformation of the intermountain seismic belt and the eastern Basin and Range province motivates an interest in continuous monitoring of the region. In this study we monitor time-lapse velocity changes within Utah and eastern Nevada using coda waves generated by repeatable explosions. This monitoring characterizes velocity changes within the region from June to September of 2007. We observe, both temporally and spatially, variable velocity changes within the monitored region, with a maximum path average velocity change of 0.2%. This suggests a significant change in the velocity within the region given the short monitoring duration. Correlation of the temporal variation of the average velocity change with strains derived from GPS-detrended displacements suggests that the velocity change might be driven by the broad deformation within the monitored region.

1. Introduction

Coda wave interferometry is an effective tool to monitor time-lapse changes within a medium, especially if these changes are weak [*Snieder et al.*, 2002]. Coda wave interferometry allows us to extract subsurface changes from scattered seismic waves generated from repeated sources. With identical sources and negligible noise, differences within the seismic coda (such as time shift and amplitude decay) provide information about the changes within the monitored medium through which the coda wave travels. Due to the redundancy in the coda waves and possibly increased illumination of the subsurface by the scattered waves, the sensitivity of the scattered waves to perturbations within the subsurface usually increases with increasing travel time. This sensitivity of the multiply scattered waves has allowed for monitoring weak changes in velocity that are in the order of 0.1% [*Snieder*, 2006]. Multiply scattered waves have successfully been used to monitor velocity changes along fault regions [*Schaff and Beroza*, 2004; *Poupinet et al.*, 1984], detect in situ velocity changes due to stress changes in a mine [*Grêt et al.*, 2006], characterize near-surface velocity changes [*Sens-Schönfelder and Wegler*, 2011; *Nakata and Snieder*, 2012], monitor temporal changes within volcanic regions [*Matsumoto et al.*, 2001], and detect far-field stress-induced velocity changes (such as those induced by solid Earth tides) [*Spane*, 2002].

The monitored region in this study covers the Basin and Range physiographic province, the transition from the Basin and Range to both the Middle Rocky Mountains and the Colorado Plateau, and the Snake River Plain (Figure 1). This region is characterized by active deformation, primary extension mostly E-W directions for the Basin and Range and more southeast to northwest extension in the Snake River Plain [*Puskas et al.*, 2007]. In addition to the major physiographic provinces, the region is characterized by mostly N-S trending normal faults, including the Wasatch fault. While there is diffuse seismicity throughout the region, most of the seismicity is concentrated with the Intermountain Seismic Belt, a zone of shallow seismicity that extends from Montana to Arizona [*Smith and Arabasz*, 1991]. Unique to western Utah are basins composed of soft sediments related to Lake Bonneville (a late Pleistocene pluvial lake). In the Salt Lake Basin these soft sediments are greater than 1 km deep in some locations [*Roten et al.*, 2011]. The soft sediments are potentially susceptible to both near-field and far-field stress loadings. Taken together, the active regional deformation, localized seismicity and faulting, and surface geology provide a complex contemporary deforming area with potentially small- and large-scale changes in both time and space.

In this study, we monitor temporal velocity changes within the crustal subsurface in the Great Basin and across the transition zone to the Middle Rocky Mountains and Colorado Plateau. We use coda waves generated by time-lapse active sources during the summer of 2007. These coda waves were recorded by USArray

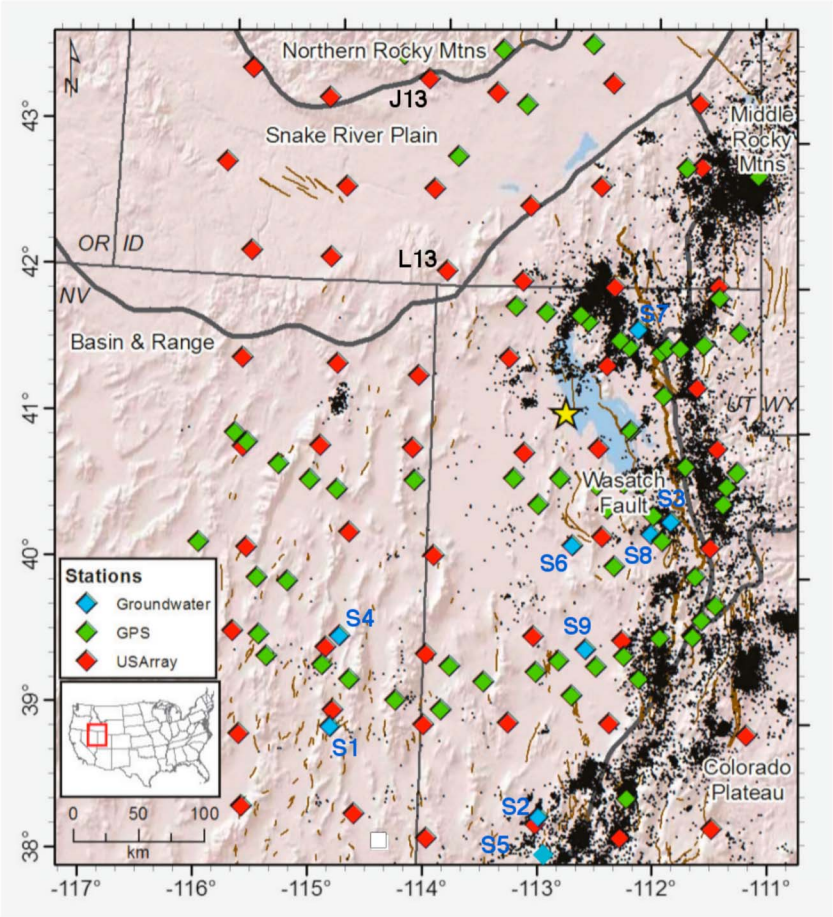

Figure 1. USArray transportable array given by the red squares. The location of the explosion (source) is given by the yellow star. The blue and the green squares give the locations of the groundwater wells and the GPS stations, respectively.

stations located in western Utah, eastern Nevada, and southern Idaho (Figure 1). In the following section, we describe in detail the data processing routine we use in this study. In sections 3 and 4 we present the results from the time-lapse monitoring of the study area and an interpretation of the results, respectively. Section 5 concludes the results of the study and discusses the assumptions we use to resolve the in situ velocity changes.

2. Data Processing

We process coda signals generated by nine rocket motor explosions, occurring between 4 June and 10 September 2007, which were surface rocket explosions at the Utah Test and Training Range of Hill Air Force Base, Utah [*Stump et al.*, 2007]. Each of the explosions was carried out at the same location with latitude and longitude of N41.141° and W112.9065°, respectively. The similarity in the source properties of the monitoring signals prevents errors in the estimated relative velocity changes due to changes in the properties of the sources (such as a shift in source location or source mechanism) generating the coda signals [*Weaver et al.*, 2011; *Kanu et al.*, 2013]. The blast signals were recorded on 54 Earthscope USArray transportable (TA) stations surrounding the blast location (Figure 1).

In this study we process the three (N-S, E-W, and vertical) components of the recorded explosive signals. Figure 2 shows an example of the unfiltered velocity records. We use a 1–5 Hz frequency band for the time-lapse monitoring, and an example blast signal for the 1–5 Hz frequency band is given in Figure 3. We use the *S* wave coda section of the signals (i.e., the section of the signal with exponential amplitude decay) (Figure 4). The onset time of the coda section after the *S* waves varies between stations. We normalize each signal with its maximum amplitude and resample each of the signals from a time interval δt of 0.025 s to

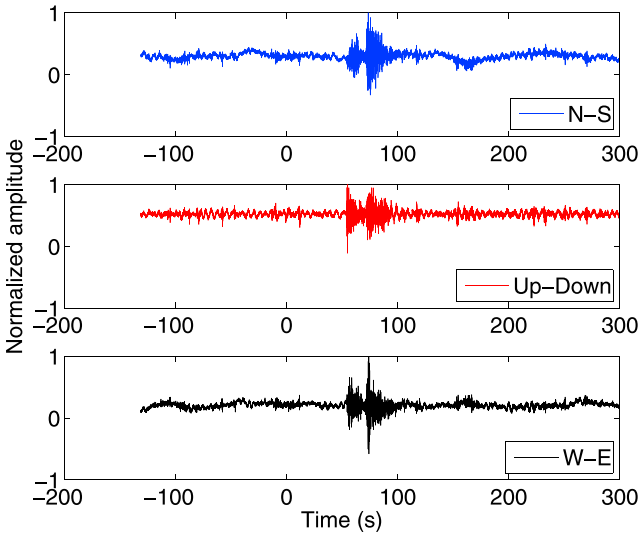

Figure 2. Example recording of typical blast events. Event 10 September 2007 recorded at station L13A. The three components, N-S (blue), Up-Down (U-D) (red), and the E-W (black) are all used in the time-lapse analysis.

0.001 s. The resampling increases the resolution of the estimated velocity changes. The data are processed using three cases of comparison. Case 1 consists of comparing each of the recorded signals to the first blast signal on 4 June. In Case 2, each signal is compared to the previous signal (in time). For Case 3, we use only the signals from 1 August to 10 September. Each of the signals in Case 3 is compared to the blast signal on 1 August. The purpose for these three cases is to check for consistency in our estimate of velocity change.

To extract the relative velocity change from the time-lapse data, we use the stretching method [*Hadziioannou et al.*, 2009]. However, rather than using the maximum correlation as the misfit function for the time-lapse objective, we use the L_2 norm as the objective function [*Kanu et al.*, 2013]. We initialize the time of the signals to the onset times of the explosive events in order to apply the stretching algorithm. A doublet consists of time-lapse signals from two explosive events. The source properties of the explosive signals are similar; therefore, any difference in the signals results from either changes along the propagation path of the signals or differences in noise properties of the signals. The major challenge we encountered while analyzing this explosive data was accounting for missing data. In some cases the data were either missing one of the components or all three of the components. We only used explosive signals that are recorded on all three components of the stations.

Because of the presence of noise in the data and because the noise becomes more prominent with increasing coda time, we only use the codas where the correlation of the early part of the coda between the time-lapse signals is greater than 0.75 and the correlation of the end of the coda is greater than 0.5 (similarity criterion). This section of the coda is submitted to the stretching algorithm. In cases where this criterion is not met, we assign zero to the relative velocity change and its error. We compute the error associated with the estimated velocity change using [*Kanu et al.*, 2013]

$$e \leq \frac{\sigma_U}{2\pi f_d A t}, \tag{1}$$

where f_d is the dominant frequency, t is the center time of the signal, A is the amplitude of the signals, and σ_U is the standard deviation of the recorded waveforms.

The estimated relative velocity changes $\langle \epsilon \rangle$ estimated in Cases 1 and 3 are cumulative velocity changes from the reference signals. However, in Case 2, the changes estimated are interval velocity changes for each monitored

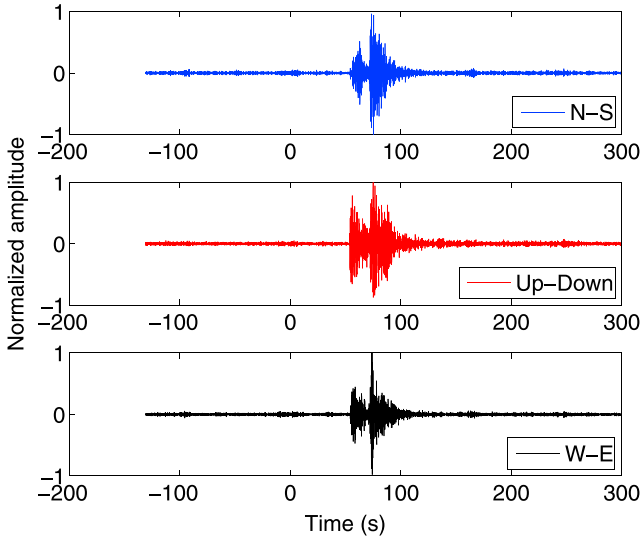

Figure 3. Typical recordings of the blast events band pass filtered between 1 and 5 Hz. The three components, N-S (blue), Up-Down (U-D) (red), and the E-W (black) are all used in the time-lapse analysis. The black rectangle gives the coda section of the blast signal.

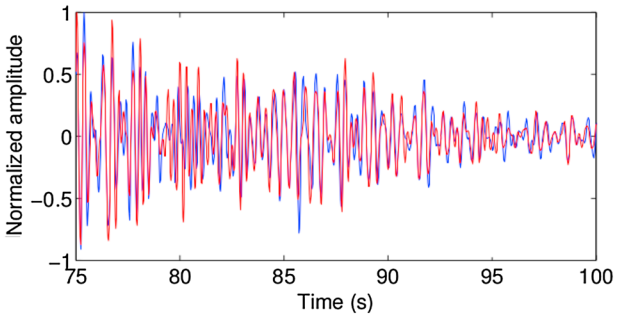

Figure 4. A typical time-lapse coda of the 1–5 Hz filtered recorded blast events for the Up-Down (U-D) component.

time period. To express the estimated velocity changes of Case 2 in a way that is consistent with the other two cases, in Figure 5 we sum the estimated velocity changes and their associated error values using the following equations and ignoring the estimates where our similarity criterion was not met:

$$\alpha_j = \sum_{i=1}^{j} \left\langle \epsilon \right\rangle_i, \tag{2}$$

and

$$e_j^{\alpha} = \sqrt{\sum_{i=1}^{j} e_i^2}, \tag{3}$$

where α is the cumulative relative velocity change, e is the error of the relative velocity change, e^{α} is the error of the cumulative relative velocity change, and i and j denote the time intervals we are monitoring with values 1 to 8.

3. Time-lapse Velocity Change

3.1. Average Velocity Changes

Figure 5 shows the cumulative estimates of the average relative velocity changes for the following: Case 1, Case 2, and Case 3. We compute the average velocity change using all the monitoring stations with estimated velocity change. Comparison of the estimated velocity changes from all three cases reveals that the estimated average velocity changes for all three components follow a consistent trend. Cases 1 and 2 show an average velocity increase of about 0.1% between 4 June and 9 July (Figure 5). Most of the 0.1% velocity change occurs between 26 June and 9 July. The temporal variation of the rest of the velocity changes lie within the error level of the velocity change. The error values are the standard deviations of the mean estimated velocity changes from all the stations. However, the velocity remains fairly constant from 9 July until 1 August. Given the consistency in the average velocity changes after 1 August shown by all the cases, the estimated velocity changes might be significant. But the variability of these velocity changes is hard to discern given the error level of the velocity changes.

3.2. Spatial Distribution of Velocity Change

Figures 6 and 7 show the velocity change for each station. The trend of the velocity changes in these figures are similar to what are observed in the average velocity changes computed using all the stations. The estimated velocity changes in Figures 6 and 7 are the estimated velocity changes in Case 2 for each time-lapse period. Figure 6 shows the spatial distribution of the velocity changes which varies with receivers; the region of dominant velocity changes also varies from one time period to the other.

The estimated velocity changes generally decrease with increasing source-receiver distance (Figure 7). The dependence of the estimated velocity change on the source-receiver distance explains the high error levels in the average of the estimated velocity change shown in Figure 5. The spread in the velocity changes estimated at the stations is not due to random errors but due to variations in the estimated velocity change among different source-receiver pairs. The spatial distribution of the velocity changes and the dependence of the velocity change on the source-receiver distance might suggest that the velocity changes in the medium are spatially localized.

3.3. Coda Time Window Analysis of $\langle \epsilon \rangle$

Obermann et al. [2013] shows that the variation of the estimated velocity change with time in the coda waves can be used to differentiate between subsurface velocity change at shallow or at great depths. We estimate velocity change within five coda time windows: $[t_s; t_s+3]$, $[t_s+5; t_s+8]$, $[t_s+10; t_s+13]$, $[t_s+15; t_s+18]$, and $[t_s + 20; t_s + 23]$, where t_s is the first arrival time of the *S* wave and the units are seconds. Figure 8 shows estimated velocity change difference Δ_T for the three signal components—N-S, E-W, and U-D components. We define the estimated velocity change difference Δ_T as

$$\Delta_T = |\langle \epsilon \rangle|_T - |\langle \epsilon \rangle|_{[t_s:t_s+3]} \tag{4}$$

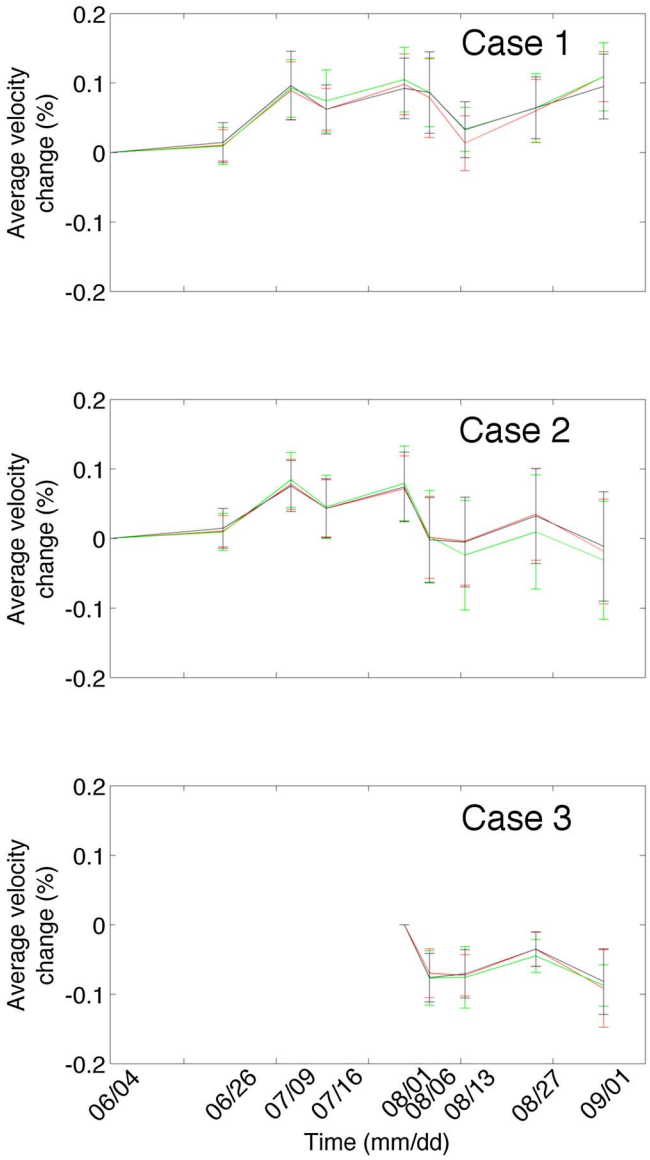

Figure 5. The cumulative relative velocity changes expressed in percentages for N-S (red), Up-Down (U-D) (green), and the E-W (black) components. Here the average is computed using all the stations in the USArray displayed in Figure 1. Missing first five estimates in Case 3 are because only signals from 1 August are processed in Case 3.

where, T is the coda time windows ($[t_s + 5; t_s + 8]$, $[t_s + 10; t_s + 13]$, $[t_s + 15; t_s + 18]$, and $[t_s + 20; t_s + 23]$ s). Figure 8 compares Δ_T for all the monitoring stations and time-lapse periods. We compute the errors using equation (3). The figure shows that the velocity change differences Δ_T are predominately negative for stations less than 50 km, but for source-receiver distances greater than 50 km the Δ_T values cluster around zero. The predominately negative values of Δ_T for source-receiver distances less than 50 km shows that the absolute value of the estimated velocity change for the coda times 5 s greater than the arrival time of S wave (t_s) are predominately smaller than the absolute value of the estimated velocity change at the coda time close to the arrival time of S wave for these distances. These negative values of Δ_T for source-receiver distances less than 50 km might indicate that the subsurface velocity change extends to the near surface [*Obermann et al.*, 2013]. However, the cluster of the Δ_T values for source-receiver distances greater than 50 km shows no consistent variations in Δ_T. This is because the estimated velocity change is fairly constant across the coda times. Figure 9 shows the estimated velocity change across the coda for the three signal components using station N12A. We estimate the velocity change using 3 s time windows with 2 s overlap. The overlap allows for more estimates of the velocity changes. The estimated velocity change is fairly constant across the coda. This variation of the estimated velocity change might suggest a broad subsurface velocity change across the crust extending to the near surface.

3.4. Parameter Estimation

Assuming a diffusion model for the coda waves, the travel time shifts (and, therefore, the estimated velocity changes) depend on the magnitude of the subsurface in situ velocity change Δv, the volume of the velocity change ΔV, the diffusion coefficient D of the scattered wave intensity [*Pacheco and Snieder*, 2005], and the source-receiver distance R_{sr}. Assuming a uniform lateral velocity change within a layer of thickness h near the Earth's free surface and 3-D bulk wave scattering, we can formulate the parametric dependence of the estimated relative velocity change $\langle \epsilon \rangle$ as follows:

$$\langle \epsilon \rangle = F(\Delta v/v, h, D, R_{sr}). \quad (5)$$

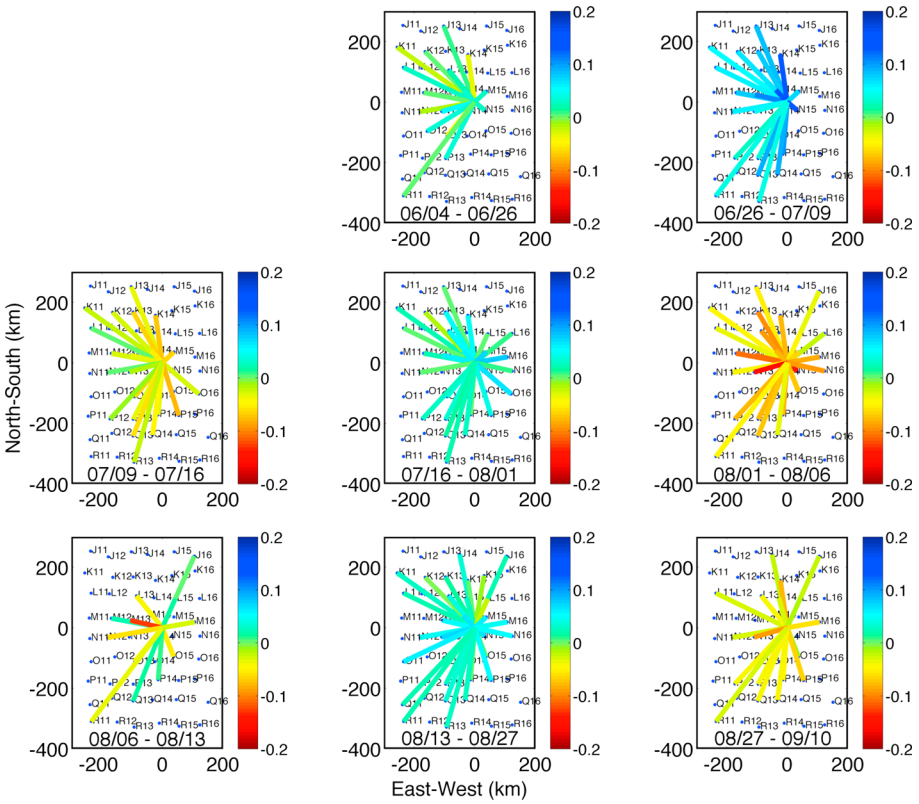

Figure 6. Relative velocity changes in percent estimated from the eight blast doublets using the vertical component of the stations. The blue points are the surface stations. The source location is the point where all the colored lines meet. The colored lines are the estimated percentage velocity changes for each source-receiver pair.

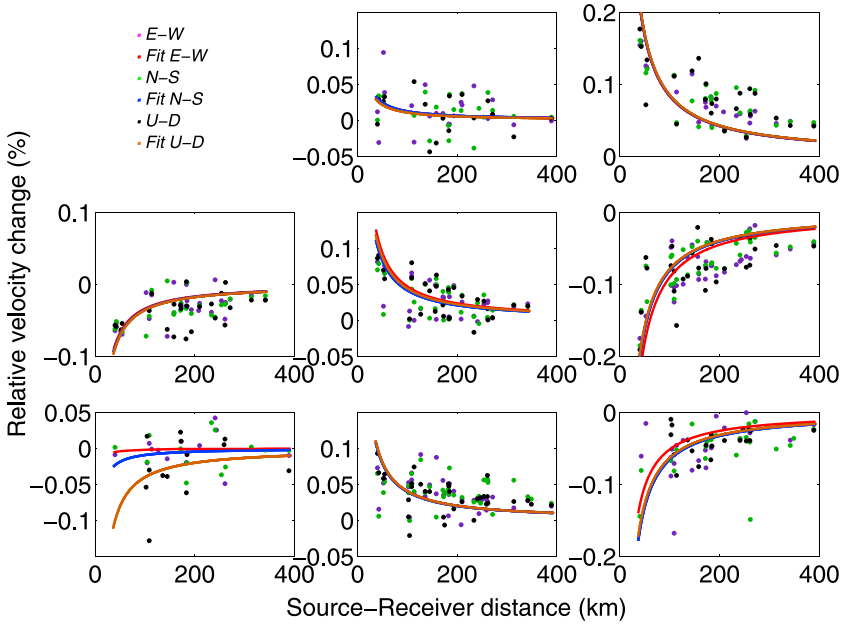

Figure 7. The relative velocity change estimated for each of the time-lapse periods as a function of source-receiver distance. Power law fitting of the estimated velocity changes in Utah Wasatch fault region. Fit E-W, N-S, and U-D are the fitting solutions for the estimated velocity changes of E-W, N-S, and U-D components, respectively.

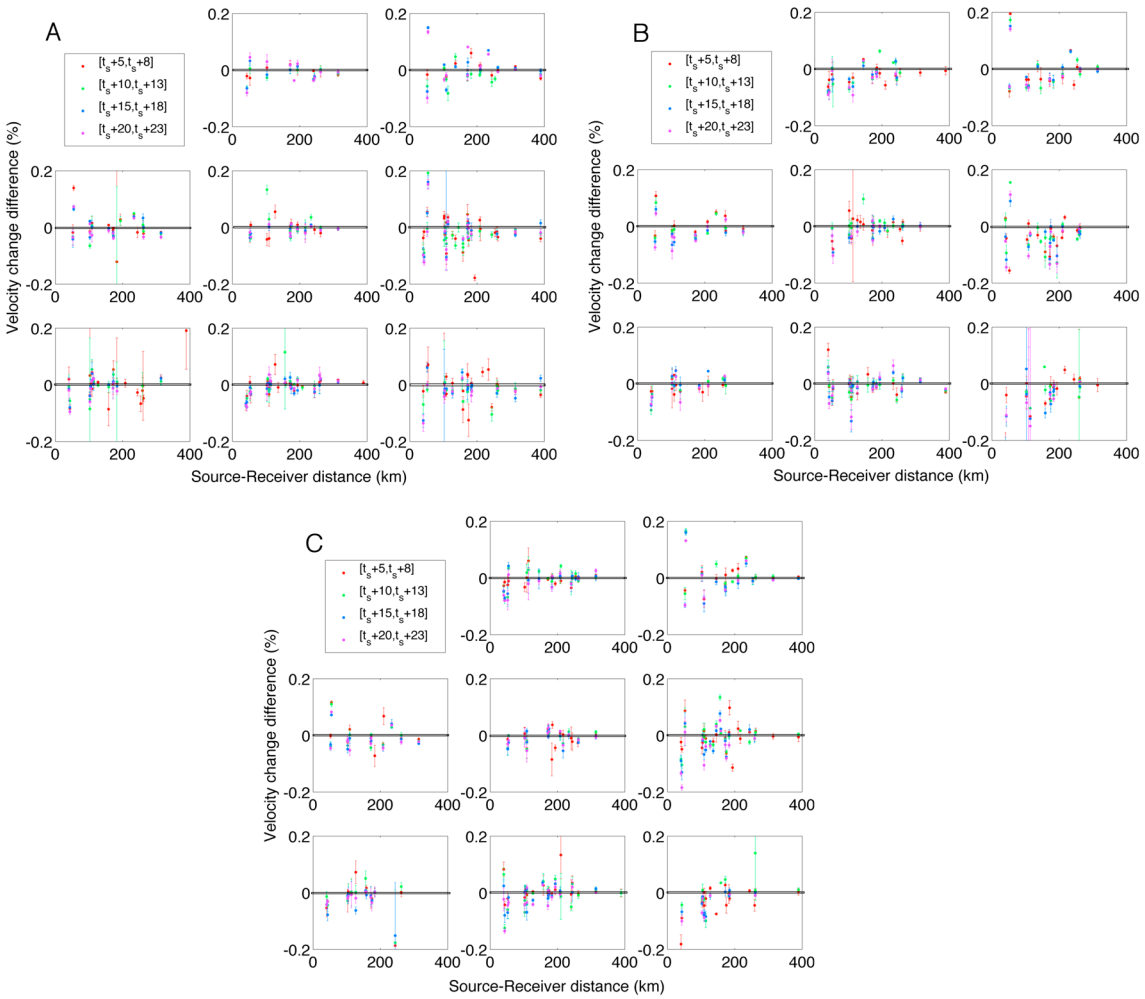

Figure 8. Estimated velocity change difference Δ_T for each time-lapse period. The plots show the estimated velocity change difference Δ_T versus the source-receiver distance for the (a) N-S component, (b) Up-Down (U-D) component, and (c) N-S component.

The function F can be found from the theory of *Pacheco and Snieder* [2005], which relates the estimated relative velocity change $\langle\epsilon\rangle$ to the model parameters ($\Delta v/v$, h, D, R_{sr}) through the relation

$$\langle\epsilon\rangle = \int_V K(\mathbf{r}, t; D)\frac{\Delta v}{v}(\mathbf{r})\,dV; \tag{6}$$

where $K(\mathbf{r}, t; D)$ is the sensitivity kernel of velocity change using multiply scattered waves, with travel time t, to subsurface relative velocity change $\Delta v/v$ at location $\mathbf{r}$. Here the source-receiver distance R_{sr} is given by the known source and receiver locations. For a given source-receiver distance R_{sr}, the estimated relative velocity change depends mostly on the parameter η, defined as

$$\eta = \frac{h}{D}\frac{\Delta v}{v}. \tag{7}$$

Figure 10 shows the apparent (estimated) velocity changes using the source-receiver distance of station J13 for values of η from 0 s/km to 0.45 s/km as obtained from equation (4). These values of η cover the range of relative velocity change that we observe in this study ($\langle\epsilon\rangle < 0.2\%$). Figure 10 suggests that the combined effect of the magnitude of the subsurface velocity change Δv and the depth of the velocity change h have the greatest influence on the estimated velocity change, for a given source-receiver distance R_{sr}. Assuming the diffusion model, different D values give different slopes in Figure 10. With a wide range of estimated velocity change $\langle\epsilon\rangle$, these different slopes suggest that diffusion coefficient D gives a weaker trade-off with the other two parameters, the magnitude of subsurface relative velocity change $\Delta v/v$ and the depth of velocity change h. However, for the range of velocity change that we estimate in this study (black rectangle

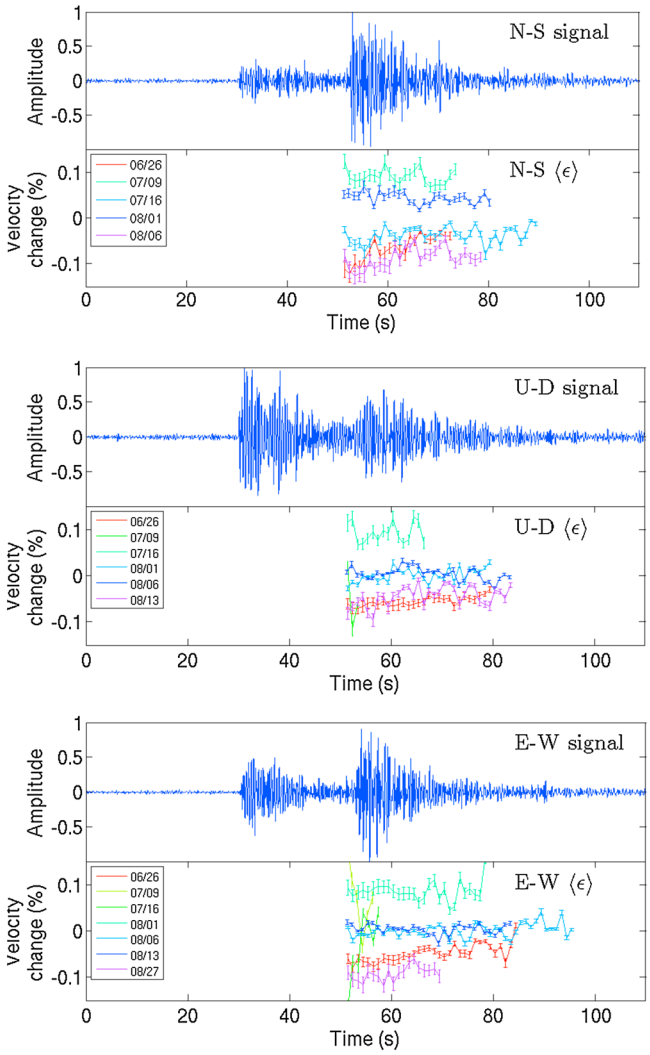

Figure 9. Estimated velocity change $\langle\epsilon\rangle$ versus time in the coda for each time-lapse period using (top) the N-S component, (middle) the Up-Down (U-D) component, and (bottom) the E-W component.

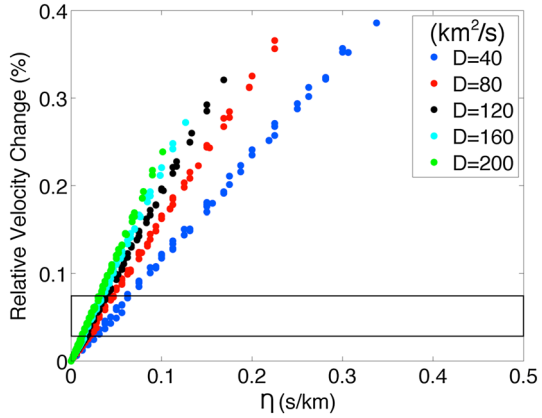

Figure 10. Dependence of the estimated velocity change on the dimensionless parameter η. The definition of η is given in equation (6). The black rectangle corresponds to the range of velocity changes estimated with station J13.

in Figure 10 for station J13), the dependence of $\langle\epsilon\rangle$ on the three parameters (h, D, $\Delta v/v$) is mostly through the combination of η. We cannot separate the effect of D except if we independently estimate D. Figure 10 is for Station J13, the other stations show a similar trade-off between the three model parameters.

We can constrain the diffusion coefficient D by using the relationship that at the peak of the coda intensity, $D = R_{sr}^2/6\langle t\rangle$ (Appendix A). The weighted average time $\langle t\rangle$ corresponds to the peak of the coda intensity. For the current data set, the estimated average diffusion coefficient is 106 km^2/s. Fixing the diffusion coefficient to this average value, the velocity change is a function of the trade-off between $\Delta v/v$ and h. The trade-off between $\Delta v/v$ and h makes it impossible to independently determine each of these parameters without additional information.

According to equation (A12) in Appendix A, we can use a power law relation to describe the dependence of estimated velocity changes on distance (Figure 7) as follows:

$$\langle\epsilon\rangle = aR_{sr}^{-1}, \tag{8}$$

where $a = (h\Delta v/v)\Sigma$ (equation (A12)). Σ is a dimensionless constant of the monitored region (equation (A11)) that depends on the diffusion coefficient D. Using the power law relation in equation (8), we invert the values of $h\Delta v/v$ from the estimated velocity changes. Table 1 gives the estimated parameters for the fitting solutions of the estimated velocity changes, the goodness of fit in R^2 (a measure of regression) values, and the inverted values of $h\Delta v/v$. We use the weighted nonlinear least squares method with the inverse of the estimated errors as weights. Negative R^2 values are encountered due to the use of a nonlinear model [*Colin Cameron and Windmeijer*, 1997]. Based on the surface layer model, the inverted values for $h\Delta v/v$ are of the order of 1% km (Table 1). This value of $h\Delta v/v$ implies, for a change extending throughout the crustal thickness of 25–40 km, the average subsurface in situ velocity becomes less than 0.04%. However, when the thickness of

Table 1. Estimated Model Parameters Using the Inverse *R* Relation

Event Period[a]	a (% km)	R^2	$h\frac{\Delta v}{v}$ (% km)
Period 1 (6/4–6/26)			
E-W	1.208 ± 4.6796	−0.0359	0.2796 ± 1.0830
N-S	1.227 ± 4.0842	−0.0244	0.2840 ± 0.9452
U-D	1.069 ± 4.9240	−0.02897	0.2474 ± 1.1396
Period 2 (6/26–7/9)			
E-W	8.272 ± 0.6536	0.3448	1.9144 ± 0.1514
N-S	8.358 ± 0.8643	−0.0987	1.9343 ± 0.2001
U-D	8.450 ± 1.1125	−0.3393	1.9556 ± 0.2576
Period 3 (7/9–7/16)			
E-W	−3.382 ± 0.3990	0.2096	−0.7827 ± 0.0924
N-S	−3.502 ± 0.4276	−0.0120	−0.8105 ± 0.0990
U-D	−3.574 ± 0.5839	−0.2823	−0.8271 ± 0.1352
Period 4 (7/16–8/1)			
E-W	4.677 ± 0.3941	0.4538	1.0824 ± 0.0913
N-S	4.141 ± 0.4903	−0.3588	0.9584 ± 0.1135
U-D	4.382 ± 0.4513	0.2150	1.0141 ± 0.1045
Period 5 (8/1–8/6)			
E-W	−9.001 ± 0.6926	0.09855	−2.0831 ± 0.1605
N-S	−8.038 ± 0.5898	0.2633	−1.8602 ± 0.1366
U-D	−7.889 ± 0.8625	-0.0293	−1.8258 ± 0.1997
Period 6 (8/6–8/13)			
E-W	−0.2111 ± 7.7143	0.00313	−0.0489 ± 1.7853
N-S	−0.9408 ± 6.9643	−0.0524	−0.2177 ± 1.6117
U-D	−4.062 ± 33.2908	0.1378	−0.9401 ± 7.7045
Period 7 (8/13–8/27)			
E-W	4.003 ± 0.5133	−0.3547	0.9264 ± 0.1188
N-S	3.949 ± 0.6128	−1.569	0.9139 ± 0.1418
U-D	4.019 ± 0.4722	0.06362	0.9301 ± 0.1093
Period 8 (8/27–9/10)			
E-W	−5.143 ± 0.9411	0.118	−1.1902 ± 0.2178
N-S	−6.538 ± 0.9513	−0.0716	−1.5131 ± 0.2202
U-D	−6.328 ± 3.2270	−0.2798	−1.4645 ± 0.7469

[a]Dates are formatted as month/day.

the layer is limited to less than a kilometer, the velocity change is large (≃ 1%). A velocity change of less than 0.04% for a crustal-scale deformation might be realistic in the actively extending Basin and Range province.

The diffusion model in Appendix A generally explains the decrease of the estimated velocity changes $\langle\epsilon\rangle$ with the source-receiver distance. However, as the goodness of fit in R^2 indicates (Table 1), equation (A12) provides a poor description of the variation of the estimated velocity changes $\langle\epsilon\rangle$ with source-receiver distance. This poor fit results from the significant scatter in the estimated velocity changes $\langle\epsilon\rangle$. The deviation of the estimated velocity changes $\langle\epsilon\rangle$ from equation (A12) can result from heterogeneity in the scattering properties of the monitored subsurface (captured by varying D values) or heterogeneity in the subsurface velocity change. These heterogeneities are ignored in the diffusion model in Appendix A.

4. Causes for the Velocity Changes

4.1. Seasonal Loading

Variations in subsurface velocity at time scales similar to the ones in the observed velocity changes might be induced by fluctuations in seasonal stress loading including precipitation, hydrological cycles, thermal changes, and groundwater level variations [*Tsai*, 2011]. Utah is a region that receives little precipitation. Available precipitation records for the monitored region show that the cumulative precipitation during the monitored time period is less than 5 cm. This amount of precipitation cannot induce the amount of velocity change observed. The groundwater level, however, can vary temporally, not only due to precipitation but also to irrigation practices [*Ashland and Giraud*, 2005], stress loading resulting from large earthquakes [*Montgomery and Manga*, 2003], and solid Earth tides [*Spane*, 2002]. Figure 11 shows the correlation between cumulative groundwater level change (positive values correspond to deepening of the groundwater level) over the monitored period with the estimated average velocity change from Case 2, using nine

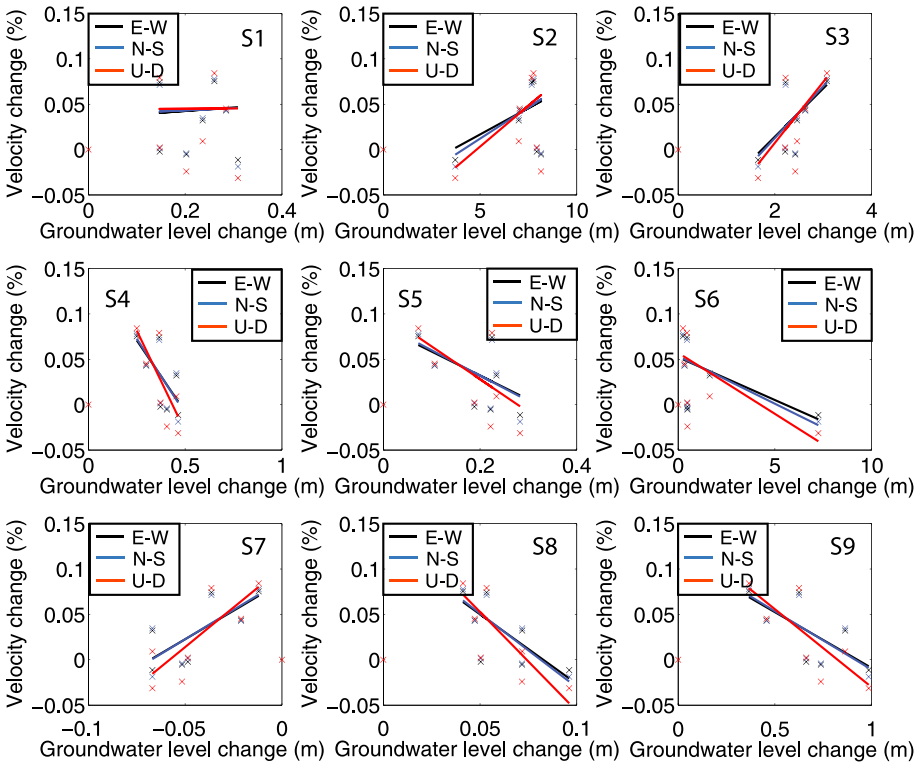

Figure 11. Correlation of average velocity change with groundwater level change measured in meters (positive meters mean deepening of the groundwater level). Each plot shows the fit of the average velocity changes from the three signal components. S1 to S9 are the names of the groundwater wells.

recording wells. The location of the recording wells of the groundwater level are shown in Figure 1. For a few of the wells (wells S4, S7, S8, and S9), a linear regression suggests that the average velocity changes show significant correlation (with regression coefficients $R^2 > 0.5$) with the groundwater level subsidence. We quantify the quality of the correlation using the R^2 values of the linear fit (Table 2) [*Draper and Smith*, 1981]. We obtain R^2 values less than 0.67 using a weighted least squares fit, where we use the standard deviation of the estimated velocity change as the weights. Among wells S4, S7, S8, and S9, only well S7 supports a direct proportional relationship between velocity change and stress (pressure) changes, if we assume that increase in groundwater level change results in an increase in effective stress. The maximum groundwater level change within the time period monitored among the wells is less than 2 m. This corresponds to approximately a change in the effective stress of less than 2.94×10^{-2} MPa assuming that the Biot coefficient is equal to 1 and a soil density of less than 2.5 g/cm^3. The stress sensitivity η reported in the literature is between 10^{-6}/Pa and 10^{-9}/Pa [*Silver et al.*, 2007; *Larose and Hall*, 2009]. These stress sensitivity values imply a range of $\Delta v/v$ values of magnitude 10^{-2} to 10^{-5}%. Given that these values of $\Delta v/v$ are orders of magnitude smaller than the estimated velocity changes $\langle \epsilon \rangle$ and that only a few of the stations show significant positive correlation with the velocity changes (Figure 11), the groundwater level change is unlikely to explain the observed velocity changes.

Table 2. Goodness of Fit Between Average Relative Velocity Changes and Groundwater (GWL) Subsidence Based on the R^2 Value (Case 2)

Velocity Components	S1	S2	S3	S4	S5	S6	S7	S8	S9
GWL stations									
E-W	−0.1866	0.0367	0.3931	0.4412	0.3179	0.1779	0.5178	0.4376	0.4798
N-S	−0.1858	0.1071	0.4697	0.4743	0.3641	0.2612	0.5366	0.5125	0.5274
U-D	−0.2493	0.0297	0.3706	0.6005	0.4117	0.2057	0.6658	0.6142	0.6357

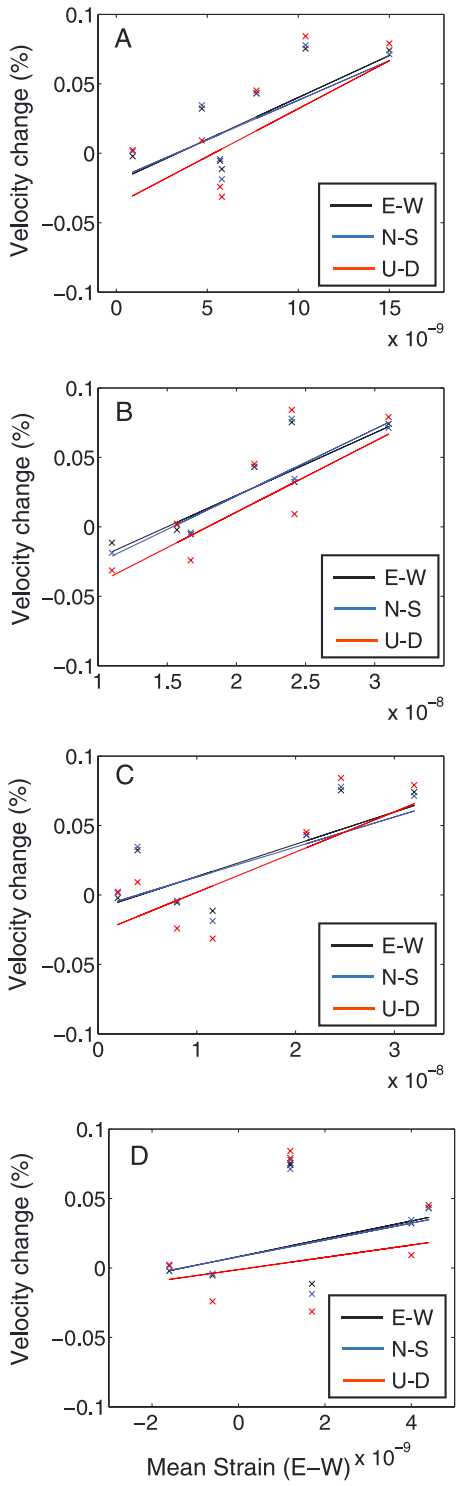

Figure 12. Linear regression between the E-W strain derived from E-W GPS-detrended displacement and the individual components of average velocity change (E-W, N-S, and vertical components). The linear regression is computed using (a) all the available GPS displacement, (b) only the Basin and Range GPS displacements, (c) only the Wasatch fault displacements, and (d) only the Snake River Plain GPS displacements.

Seasonal strain changes can be recorded by detrended GPS displacement measurements. Using horizontal GPS displacements from GPS stations within our monitored region (Figure 1), we quantify the correlation between the estimated relative velocity change and the seasonal E-W strain using the R^2 values of the linear fit (Figure 12). We compute the average horizontal strain between stations using the average-detrended horizontal GPS displacements denoted by $d_k^{i,j}$. Because, the horizontal distances between the stations are much larger than the elevations between the stations, we approximate the average horizontal strains by

$$\gamma_{kk}^{ij} = \frac{d_k^j - d_k^i}{X_k^j - X_k^i}, \tag{9}$$

where i and j are station indexes, X_k is either E-W ($k = 1$) or N-S ($k = 2$) GPS location, and γ is the average strain. The detrended GPS displacement $d_k^{i,j}$ is averaged 2 days prior to and 2 days after the time of each blast. Table 3 and Figure 12 show the linear correlation with the estimated average velocity changes using four groups of the GPS stations. One group consists of all the available GPS stations, while the other three groups use either only stations within the Snake River Plain, only stations within the Basin and Range, or only the stations close to the Wasatch fault. Comparison of the estimated average velocity changes from Case 2 with the average horizontal GPS strain, using all the GPS stations, shows a significant linear correlation, based on the R^2 values of the velocity changes with the E-W strain (Table 3). For the strains derived from the Basin and Range GPS stations, there is a larger correlation of the velocity changes with the E-W strains compared to the strain derived from all the stations. Stations along the Snake River Plain region show negligible correlation ($R^2 < 0.23$) with the observed velocity change (Figure 12d and Table 3). Fits with negative R^2 values here suggest that the linear fit might be an incorrect model for those fits.

Seasonal variation in GPS displacement and therefore the seasonal variations in the strain can be induced by thermoelastic or hydrologic variations [*Tsai*, 2011]. While hydrologic variations can induce localized changes, variations in the thermal conditions within the crust can be responsible for a broad crustal deformation [*Lachenbruch and Sass*, 1977]. Crustal deformation in the Basin and Range predominately creates normal fault and extensive structures striking in approximately N-S orientations. The correlation between the estimated average velocity changes and the calculated strain changes suggests that the velocity changes might be driven at least in part by the changes in the seasonal strain. With the inconsistent correlation we obtained between the average velocity and the groundwater level change, the strain changes here might be driven by tectonic or thermoelastic stress

Table 3. Goodness of Fit Between Average Relative Velocity Changes and Seasonal Variation of (Detrended) GPS Displacement Based on the R^2 Value (Case 2)

GPS Component | Velocity Components	E-W	N-S	U-D
All GPS stations			
E-W	0.6106	0.5228	0.4993
N-S	−0.1240	−0.1401	−0.1828
Basin and Range stations			
E-W	0.7842	0.7982	0.6354
N-S	−0.1424	−0.1545	−0.1952
Wasatch fault stations			
E-W	0.6335	0.5442	0.6267
N-S	0.1476	0.1912	0.0750
Snake River Plain stations			
E-W	0.2261	−0.0052	−0.1200
N-S	−0.1127	−0.1491	−0.0770

changes. Given that the observed velocity changes correlate significantly with the strains aligned in the direction of the crustal deformation in the area, the velocity changes we observe might extend deep into the crust and therefore result in a small subsurface $\Delta v/v$. If the seasonal strains from the Basin and Range GPS-detrended displacements are induced by crustal deformation, a significant part of the velocity change observed might be driven by broad crustal deformation in the monitored region. The monitored region covers the eastern flank of the Basin and Range, which has been shown to have elevated thermal conditions [*Eaton*, 1982] that might be responsible for broad active deformation in the region. Tectonic deformation of the region could induce velocity changes within the crust; however, these velocity changes are broader, more gradual, and extend deeper than the change due to other physical mechanisms such as variations in groundwater level or regional seismicity. Because of the broad and gradual properties of the crustal deformation-induced velocity changes, we expect larger values of h (volume of change) and lower subsurface relative velocity changes $\Delta v/v$. With a larger value of h, crustal deformation due to stress changes or elevated temperatures deep within the crust might explain, at least in part, the inverted values of $h\Delta v/v$ on the order of 1% km.

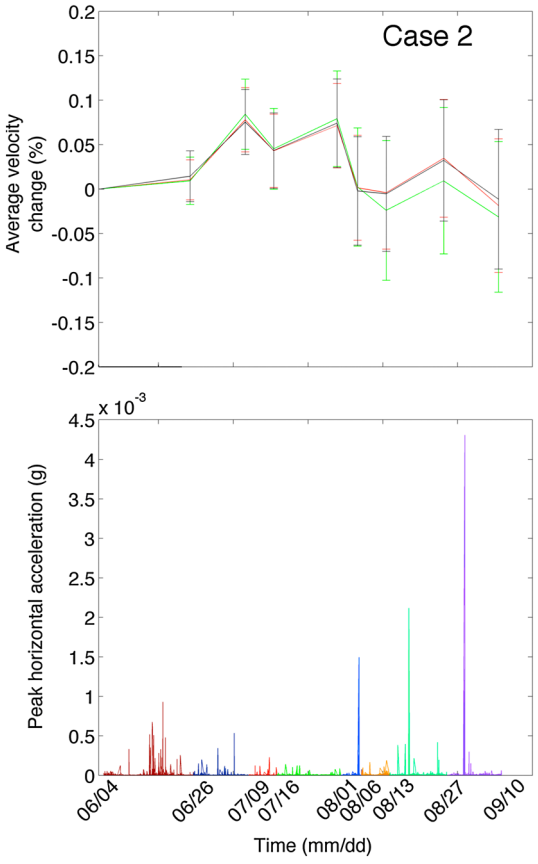

Figure 13. Comparison of the peak ground acceleration (PGA) with average relative velocity change estimated in Case 2. The PGA values are estimated from the local seismicity (M > −0.36) that occurred during the monitored time-lapse period. The PGA values are estimated using relationship between PGA and the magnitude of an earthquake [*Chiou et al.*, 2010].

4.2. Local Seismicity

Figure 13 shows the peak ground acceleration (PGA) due to local seismicity and the estimated velocity changes. We compute PGA (y) using its relationship with event magnitude given by *Chiou et al.* [2010]:

$$\ln(y) = \ln(y_{\text{ref}}) + \phi \ln(V_{s30}) + f_{\text{NL}}(V_{s30}, y_{\text{ref}}) \quad (10)$$

where $\ln(y_{\text{ref}}) = c_1 - 2.1 \ln[R_f + C_{\text{NS}}] + (-0.5 + 2.1) \ln\sqrt{R_f + 50^2} + \gamma R_f$ and $C_{\text{NS}} = c_5 \cosh[c_6 \max(M - 3.0)]$. V_{s30} is the

Table 4. Goodness of Fit Between Relative Velocity Change and PGA Based on the R^2 Value (Case 2)

Velocity Components	Total PGA Soil	Mean PGA Soil
E-W	0.2186	−0.0208
N-S	0.3158	0.0504
U-D	0.2060	0.0472

average shear wave velocity in the top 30 m, f_{NL} defines the nonlinear soil response of the monitored area, M is the event magnitude, and R_f is the distance to the fault rupture location in kilometers. We use values for coefficients ϕ, γ, c_1, c_5, and c_6 reported by *Pankow* [2000] for the Utah region. To compute PGA, we use the V_{s30} value of 230 m/s. The deviation of V_{s30} for each monitoring station from 230 m/s will affect the magnitude of the PGA values and will affect negligibly the temporal variations of the PGA values. The temporal variations of the PGA values depend on the number and magnitude of the seismicity registered during each time period. We compute PGA for earthquake magnitudes and hypocenter parameters determined by the Utah Regional Seismic Network for seismic events in the monitoring region during the monitored time-lapse period (Figure 1).

The following time intervals contain days of relatively high spikes of PGA events: 1–6 August, 13–27 August, and 27 August to 10 September (Figure 13). Among these time periods, only the time period—27 August to 10 September—has the anomalous PGA events occurring near the end of each time-lapse period. Comparing the PGA values with the estimated average velocity change, there is no clear correlation between the local seismicity induced PGA and the estimated average velocity changes. This insignificant correlation is suggested by the R^2 value of the linear fit between the PGA (total and average) values and the estimated average velocity changes (Table 4). The R^2 value of the linear fit for each of the average velocity changes is less than 0.32.

The effect of the local seismicity is expected to be constrained near the Wasatch fault, which is situated in the eastern section of the monitored region. Therefore, local seismicity within the Wasatch fault system might be an unlikely cause for the observed velocity changes.

5. Discussion and Conclusions

The estimated velocity changes suggest that the eastern flank of the Basin and Range and the transition to the Middle Rocky Mountains and Colorado Plateau are undergoing small but significant velocity changes within a short period of time. Correlation of the estimated velocity changes with groundwater level changes, seasonal tectonic strain changes, and local seismicity indicates that the velocity change mostly might be induced by the E-W crustal deformation in the eastern Basin and Range. The magnitude of the estimated average velocity change varies from one time-lapse period to the other. The maximum of the absolute value of the estimated velocity change is 0.2%. Due to the averaging effect of coda interferometry, the volume and the magnitude of the velocity change are strongly correlated. We observe that the path-averaged velocity changes depend on the distance between the monitoring source and receivers. The estimated velocity changes generally decrease with source-receiver distance R_{sr}. This reduction in the estimated velocity change with source-receiver distance is seen assuming 3-D diffusion wave scattering. With the diffusion model and assuming a uniform scattering model, there is an inverse R_{sr} dependence of the estimated velocity changes $\langle\epsilon\rangle$. However, there is significant deviation of the estimated velocity changes $\langle\epsilon\rangle$ from the inverse R_{sr} relation. This deviation can result from heterogeneities in the subsurface $\Delta v/v$ or in the scattering properties of the subsurface. To obtain the inverse R_{sr} relation and consequently estimate the magnitude of the subsurface in situ velocity change using the coda waves, we have made the following simplifying assumptions:

First, we assume that the coda waves we use for the time-lapse monitoring are described using the diffusion approximation for multiply scattered waves. This approximation is usually an oversimplification of the scattered waves especially in the early part of the coda. This approximation is likely to result in an erroneous estimation of the inverted values of $h\Delta v/v$. Also, we assume a uniform diffusion model for the monitored area defined by an average diffusion constant in the subsurface. This diffusion constant is related to the distance between source and receivers using the diffusion model of the recorded intensities. If the average diffusion constant is uncharacteristic of the variation of the diffusion property of the monitored region, the inverted $h\Delta v/v$ will also be erroneous.

Second, we use a semiinfinite 3-D subsurface with a fully reflecting free surface to invert for $h\Delta v/v$. The fully reflecting free surface may be a fair approximation of the free surface, but we ignore the presence of the

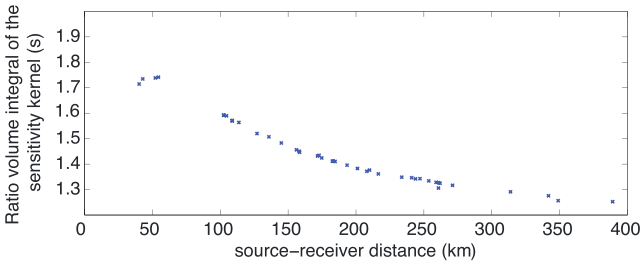

Figure 14. Increased sensitivity due to the presence of Moho interface at depth 25 km based on the ratio of the volume integral of the sensitivity kernel with and without the Moho interface.

Moho discontinuity. This boundary will change the magnitude of the sensitivity kernel of the coda because the crustal thickness is much less than the source-receiver distances used in estimating the velocity changes. *Keller et al.* [1975] suggest that the crustal Basin and Range-Colorado Plateau transition has a thickness of about 25 km with a crustal thickness of 30 km for the Basin and Range [*Gilbert and Sheehan*, 2004]. Assuming an absorbing boundary at the crust-upper mantle interface will likely increase the magnitude of the sensitivity kernel [*Rossetto et al.*, 2011]. Figure 14 shows that with a Moho interface at 25 km, the volumetric integral of the sensitivity kernel is increased by a factor of 1.25 to 1.80, depending on the source-receiver distance. This will result in a reduction of the value of the inverted $h\Delta v/v$.

Third, we made a 2-D approximation of the expression of *Pacheco and Snieder* [2005] in equation (A6) by assuming that $h/R_{sr} \ll 1$. Therefore, the inverted $h\Delta v/v$ represents the true $h\Delta v/v$ within the subsurface if the velocity changes are restricted within the crust. If the observed velocity changes result from a deeper region of the subsurface, then the true values of $h\Delta v/v$ might deviate from the inverted values. Because of the large values of R_{sr} (several hundred kilometers), the approximation of $h/R_{sr} \ll 1$ is not likely to significantly affect the inverted values of $h\Delta v/v$.

Fourth, due to the extent of the monitored region, the recorded explosive signals are expected to generate surface waves. Due to conversion from body waves to surface waves, the surface waves can arrive within the coda wave time window especially for short source-receiver distances. In the recorded explosive signals, the surface waves mostly arrive after the coda waves. However, the relative arrival times of the coda wave and the surface wave are dependent on the source-receiver distances. In this study we have restricted the velocity changes analysis to the coda wave. The variation of the estimated velocity change across the coda (Figure 9) does not suggest a significant presence or contribution of surface-dominated scattered wave [*Obermann et al.*, 2013]. However, the presence of surface wave or surface dominated scattered waves in the coda will increase the sensitivity of the scattered waves to localized velocity change. This will result in lower values of $h\Delta v/v$. Therefore, the inverted $h\Delta v/v$ values can be considered as the upper limit of the real $h\Delta v/v$ changes within the monitored region.

Finally, we assume a uniform lateral velocity change in the layer of velocity change across the monitored region. In reality it is likely that the velocity changes are localized in space both laterally and in depth. A heterogeneity in the subsurface velocity change likely explains the scatter in the estimated velocity changes. The inverted $h\Delta v/v$ can be seen as the average $h\Delta v/v$ of the true $h\Delta v/v$ within the monitored region. This means that in some areas of the monitored region, the true changes will be higher or lower than the inverted values.

The above assumptions notwithstanding, the estimated velocity changes suggest that the crust underneath the region around the eastern Basin and Range is undergoing a path-averaged velocity change of the order of 0.1% within a short period of time. There might be a need to incorporate these velocity changes in any characterization of both the seismicity and deformation within the region. However, it would be useful to discern if these velocity changes are seasonal by incorporating measurements taken over several years or by applying coda wave interferometry to the coda waves generated from ambient noise correlations [*Hadziioannou et al.*, 2009; *Sens-Schönfelder and Wegler*, 2011].

Appendix A: Analytical Approximation of the Model of *Pacheco and Snieder* [2005]

The time shift $\langle\tau(t)\rangle$ extracted from repeating coda (assuming the diffusion model) can be related to the localized velocity changes by the model of *Pacheco and Snieder* [2005] as

$$-\frac{\langle\tau(t)\rangle}{t} = \langle\epsilon(t)\rangle = \int_V \frac{K(\mathbf{s},\mathbf{x_o},\mathbf{r},t)}{t}\frac{\Delta v}{v}(\mathbf{x_o})\,dV, \tag{A1}$$

where V is the integration volume and $\mathbf{s}$, $\mathbf{x_o}$, and $\mathbf{r}$ are the source, arbitrary, and receiver locations, respectively. The sensitivity kernel $K(\mathbf{s}, \mathbf{x_o}, \mathbf{r}, t)$ is

$$K(\mathbf{s}, \mathbf{x_o}, \mathbf{r}, t) = \frac{\int_0^t P(\mathbf{s}, \mathbf{x_o}, t')P(\mathbf{x_o}, \mathbf{r}, t - t')\,\mathrm{d}t'}{P(\mathbf{s}, \mathbf{r}, t)}, \tag{A2}$$

and $P(\mathbf{x}_1, \mathbf{x}_2, t)$ is the normalized intensity recorded at a receiver location x_2 due to a source at x_1. Using the diffusion approximation for the normalized intensity in a 3-D semiinfinite inhomogeneous medium with a full reflecting surface boundary and where the source and receivers are located on the boundary, the normalized intensity is [*Rossetto et al.*, 2011]

$$P(R, t) = \frac{2}{(4\pi Dt)^{3/2}} \exp\left(-\frac{R_{sr}^2}{4Dt}\right). \tag{A3}$$

Then the sensitivity kernel $K(\mathbf{s}, \mathbf{x_o}, \mathbf{r}, t)$ in a 3-D medium with a full reflecting surface boundary is given by [*Rossetto et al.*, 2011]

$$K(\mathbf{s}, \mathbf{x_o}, \mathbf{r}, t) = \frac{1}{2\pi D} \exp\left(\frac{R_{sr}^2 - (r+s)^2}{4Dt}\right)\left(\frac{1}{s} + \frac{1}{r}\right), \tag{A4}$$

where R_{sr} is the source-receiver distance and r and s are distances from the receiver and source to $\mathbf{x_o}$, respectively. Therefore, from equation (A1),

$$-\frac{\langle\tau(t)\rangle}{\langle t\rangle} = \langle\epsilon(t)\rangle = \int_x\int_y\int_0^h \frac{1}{2\pi D\langle t\rangle} \exp\left(\frac{R_{sr}^2 - (r+s)^2}{4D\langle t\rangle}\right)\left(\frac{1}{s} + \frac{1}{r}\right)\frac{\Delta v}{v}(\mathbf{x_o})\,\mathrm{d}z\,\mathrm{d}y\,\mathrm{d}x. \tag{A5}$$

Assuming $h/R_{sr} << 1$ and that the relative velocity change is constrained to the near-surface slab such that $\Delta v/v(\mathbf{x_o}) = \Delta v/v$, then

$$-\frac{\langle\tau(t)\rangle}{\langle t\rangle} = \langle\epsilon(t)\rangle \simeq h\frac{\Delta v}{v}\int_x\int_y \frac{1}{2\pi D\langle t\rangle} \exp\left(\frac{R_{sr}^2 - (r+s)^2}{4D\langle t\rangle}\right)\left(\frac{1}{s} + \frac{1}{r}\right)\mathrm{d}y\,\mathrm{d}x. \tag{A6}$$

The travel time $\langle t\rangle$ associated with the estimated average velocity $\langle\epsilon(t)\rangle$ is [*Snieder*, 2006]

$$\langle t\rangle = \frac{\int_{t'} w(t)t\,\mathrm{d}t'}{\int_{t''} w(t)\,\mathrm{d}t'}, \tag{A7}$$

where $w(t)$ is the intensity of the scattered waves. Because the intensity is higher in the early part of the coda rather than in the later, the weighted average time $\langle t\rangle$ lies close to the peak of the intensity. At the intensity peak,

$$\frac{\partial P(R_{sr}, t)}{\partial t} = 0. \tag{A8}$$

Based on equation (A3), $R_{sr}^2/6D\langle t\rangle = 1$.

In order to define equation (A6) with the major contributing variables, we express the variables as dimensionless quantities, let $x' = x/\sqrt{6D\langle t\rangle}$, $y' = y/\sqrt{6D\langle t\rangle}$, $R'_{sr} = R_{sr}/\sqrt{6D\langle t\rangle} = 1$, $r' = r/\sqrt{6D\langle t\rangle}$, and $s' = s/\sqrt{6D\langle t\rangle}$. Then,

$$-\frac{\langle\tau(t)\rangle}{\langle t\rangle} = \langle\epsilon(t)\rangle \simeq \frac{h}{\pi}\frac{\Delta v}{v}\sqrt{\frac{3}{2D\langle t\rangle}}\int_{x'}\int_{y'} \exp\left(\frac{3}{2}\left(1 - (r'+s')^2\right)\right)\left(\frac{1}{s'} + \frac{1}{r'}\right)\mathrm{d}y'\,\mathrm{d}x'. \tag{A9}$$

Using $R_{sr}^2/6D\langle t\rangle = 1$, equation (A9) gives

$$-\frac{\langle\tau(t)\rangle}{\langle t\rangle} = \langle\epsilon(t)\rangle \simeq \frac{3}{\pi}\frac{h}{R_{sr}}\frac{\Delta v}{v}\int_{x'}\int_{y'} \exp\left(\frac{3}{2}\left(1 - (r'+s')^2\right)\right)\left(\frac{1}{s'} + \frac{1}{r'}\right)\mathrm{d}y'\,\mathrm{d}x'. \tag{A10}$$

Let

$$\frac{3}{\pi}\int_{x'}\int_{y'} \exp\left(\frac{3}{2}\left(1 - (r'+s')^2\right)\right)\left(\frac{1}{s'} + \frac{1}{r'}\right)\mathrm{d}y'\,\mathrm{d}x' = \Sigma, \tag{A11}$$

Acknowledgments
We are grateful for the financial support of the Department of Energy (DOE) through grant DE-EE0002758. The explosive signals used in this study were obtained from the broadband USArray stations via IRIS.

then

$$-\frac{\langle \tau(t) \rangle}{\langle t \rangle} = \langle \epsilon(t) \rangle \simeq \frac{h}{R_{sr}} \frac{\Delta v}{v} \Sigma. \quad \text{(A12)}$$

Equation (A12) allows for a parametric description of the estimated velocity change $\langle \epsilon(t) \rangle$ in terms of the model parameters h, $\Delta v/v$, and R_{sr}. Σ is a constant dimensionless parameter, and the numerical solution for our study is equal to 4.32 ± 0.02. The error in Σ is a numerical error.

References

Ashland, X., and R. E. Giraud (2005), *Groundwater Level Fluctuations in Wasatch Front Landslides and Adjacent Slopes, Northern Utah*, vol. 448, Open-File Rep., 22 pp., Utah Geol. Surv., Salt Lake City, Utah.

Chiou, B., R. Youngs, N. Abrahamson, and K. Addo (2010), Ground-motion attenuation model for small-to-moderate shallow crustal earthquakes in California and its implications on regionalization of ground-motion prediction models, *Earthquake Spectra*, *26*(4), 907–926, doi:10.1193/1.3479930.

Colin Cameron, A., and F. A. Windmeijer (1997), An R-squared measure of goodness of fit for some common nonlinear regression models, *J. Econometrics*, *77*(2), 329–342, doi:10.1016/S0304-4076(96)01818-0.

Draper, N. R., and H. Smith (1981), *Applied Regression Analysis*, Wiley, New York.

Eaton, G. P. (1982), The Basin and Range province: Origin and tectonic significance, *Annu. Rev. Earth Planet. Sci.*, *10*, 409–440, doi:10.1146/annurev.ea.10.050182.002205.

Gilbert, H. J., and A. F. Sheehan (2004), Images of crustal variations in the intermountain west, *J. Geophys. Res.*, *109*, B03306, doi:10.1029/2003JB002730.

Grêt, A., R. Snieder, and U. Özbay (2006), Monitoring in situ stress changes in a mining environment with coda wave interferometry, *Geophys. J. Int.*, *167*(2), 504–508, doi:10.1111/j.1365-246X.2006.03097.x.

Hadziioannou, C., E. Larose, O. Coutant, P. Roux, and M. Campillo (2009), Stability of monitoring weak changes in multiply scattering media with ambient noise correlation: Laboratory experiments, *J. Acoust. Soc. Am.*, *125*(6), 3688–3695, doi:10.1121/1.3125345.

Kanu, C. O., R. Snieder, and D. O'Connell (2013), Estimation of velocity change using repeating earthquakes with different locations and focal mechanisms, *J. Geophys. Res. Solid Earth*, *118*, 2905–2914, doi:10.1002/jgrb.50206.

Keller, G. R., R. B. Smith, and L. W. Braile (1975), Crustal structure along the Great Basin-Colorado Plateau transition from seismic refraction studies, *J. Geophys. Res.*, *80*(8), 1093–1098, doi:10.1029/JB080i008p01093.

Lachenbruch, A. H., and J. H. Sass (1977), Heat flow in the United States and the thermal regime of the crust, in *The Earth'S Crust, Geophys. Monogr. Ser.,* vol. 20, edited by J. G. Heacock et al., pp. 626–675, doi:10.1029/GM020p0626.

Larose, E., and S. Hall (2009), Monitoring stress related velocity variation in concrete with a 2×10^{-5} relative resolution using diffuse ultrasound, *J. Acoust. Soc. Am.*, *125*(4), 1853, doi:10.1121/1.3079771.

Matsumoto, S., K. Obara, K. Yoshimoto, T. Saito, A. Ito, and A. Hasegawa (2001), Temporal change in *P*-wave scatterer distribution associated with the *M*6.1 earthquake near Iwate Volcano, northeastern Japan, *Geophys. J. Int.*, *145*(1), 48–58, doi:10.1111/j.1365-246X.2001.00339.x.

Montgomery, D. R., and M. Manga (2003), Streamflow and water well responses to earthquakes, *Science*, *300*(5628), 2047–2049, doi:10.1126/science.1082980.

Nakata, N., and R. Snieder (2012), Estimating near-surface shear wave velocities in Japan by applying seismic interferometry to KiK-net data, *J. Geophys. Res.*, *117*, B01308, doi:10.1029/2011JB008595.

Obermann, A., T. Planès, E. Larose, C. Sens-Schönfelder, and M. Campillo (2013), Depth sensitivity of seismic coda waves to velocity perturbations in an elastic heterogeneous medium, *Geophys. J. Int.*, *194*(1), 372–382.

Pacheco, C., and R. Snieder (2005), Time-lapse travel time change of multiply scattered acoustic waves, *J. Acoust. Soc. Am.*, *118*(3), 1300–1310, doi:10.1121/1.2000827.

Pankow, K. L. (2000), Instrumentally recorded ground motions in the Utah Region since, in *Selected Topics in Engineering and Environmetal Geology in Utah: Utah Geological Association Publication*, vol. 41, p. 2012, Utah Geological Association, Salt Lake City, Utah.

Poupinet, G., W. L. Ellsworth, and J. Frechet (1984), Monitoring velocity variations in the crust using earthquake doublets: An application to the Calaveras fault, California, *J. Geophys. Res.*, *89*(B7), 5719–5731, doi:10.1029/JB089iB07p05719.

Puskas, C. M., R. B. Smith, C. M. Meertens, and W. L. Chang (2007), Crustal deformation of the Yellowstone-Snake river plain volcano-tectonic system: Campaign and continuous GPS observations, 1987–2004, *J. Geophys. Res.*, *112*, B03401, doi:10.1029/2006JB004325.

Rossetto, V., L. Margerin, T. Planès, and E. Larose (2011), Locating a weak change using diffuse waves: Theoretical approach and inversion procedure, *J. Appl. Phys.*, *109*(3), 903–911, doi:10.1063/1.3544503.

Roten, D., K. B. Olsen, J. C. Pechmann, V. M. Cruz-Atienza, and H. Magistrale (2011), 3D simulations of *M* 7 earthquakes on the Wasatch fault, Utah. Part I: Long-period (0–1 Hz) ground motion, *Bull. Seismol. Soc. Am.*, *101*(5), 2045–2063, doi:10.1785/0120110031.

Schaff, D. P., and G. C. Beroza (2004), Coseismic and postseismic velocity changes measured by repeating earthquakes, *J. Geophys. Res.*, *109*, B10302, doi:10.1029/2004JB003011.

Sens-Schönfelder, C., and U. Wegler (2011), Passive image interferometry for monitoring crustal changes with ambient seismic noise, *C. R. Geosci.*, *343*(8-9), 639–651, doi:10.1016/j.crte.2011.02.005.

Silver, P. G., T. M. Daley, F. Niu, and E. L. Majer (2007), Active source monitoring of cross-well seismic travel time for stress-induced changes, *Bull. Seismol. Soc. Am.*, *97*(1B), 281–293, doi:10.1785/0120060120.

Smith, R. B., and W. J. Arabasz (1991), Seismicity of the intermountain seismic belt, in *Neotectonics of North America*, Decade Map vol. 1, pp. 185–228, Geol. Soc. Am.

Snieder, R. (2006), The theory of coda wave interferometry, *Pure Appl. Geophys.*, *163*(2-3), 455–473, doi:10.1007/s00024-005-0026-6.

Snieder, R., A. Grêt, H. Douma, and J. Scales (2002), Coda wave interferometry for estimating nonlinear behavior in seismic velocity, *Science*, *295*(5563), 2253–2255, doi:10.1126/science.1070015.

Spane, F. A. (2002), Considering barometric pressure in groundwater flow investigations, *Water Resour. Res.*, *38*(6), 1–18, doi:10.1029/2001WR000701.

Stump, B., et al. (2007), Seismic and infrasonic energy generation and propagation at local and regional distances: Phase I—Divine Strake Experiment, *Air Force Research Laboratory report, AFRL-RV-HA-TR-2007-1188*.

Tsai, V. C. (2011), A model for seasonal changes in GPS positions and seismic wave speeds due to thermoelastic and hydrologic variations, *J. Geophys. Res.*, *116*, B04404, doi:10.1029/2010JB008156.

Weaver, R. L., C. Hadziioannou, E. Larose, and M. Campillo (2011), On the precision of noise correlation interferometry, *Geophys. J. Int.*, *185*(3), 1384–1392, doi:10.1111/j.1365-246X.2011.05015.x.